Na+-dependent gate dynamics and electrostatic attraction ensure substrate coupling in glutamate transporters.

C Alleva, Kirill Kovalev, R Astashkin, M Berndt, C Baeken, T Balandin, Valentin Gordeliy, Ch Fahlke, J-P Machtens

STRUCTURAL BIOLOGY

Na$^+$-dependent gate dynamics and electrostatic attraction ensure substrate coupling in glutamate transporters

C. Alleva[1]*, K. Kovalev[1,2,3,4,5,6]*, R. Astashkin[2,4], M. I. Berndt[1], C. Baeken[3,6], T. Balandin[3,6], V. Gordeliy[2,3,4,6], Ch. Fahlke[1,4†‡], J.-P. Machtens[1,7†‡]

Excitatory amino acid transporters (EAATs) harness [Na$^+$], [K$^+$], and [H$^+$] gradients for fast and efficient glutamate removal from the synaptic cleft. Since each glutamate is cotransported with three Na$^+$ ions, [Na$^+$] gradients are the predominant driving force for glutamate uptake. We combined all-atom molecular dynamics simulations, fluorescence spectroscopy, and x-ray crystallography to study Na$^+$:substrate coupling in the EAAT homolog Glt$_{Ph}$. A lipidic cubic phase x-ray crystal structure of wild-type, Na$^+$-only bound Glt$_{Ph}$ at 2.5-Å resolution revealed the fully open, outward-facing state primed for subsequent substrate binding. Simulations and kinetic experiments established that only the binding of two Na$^+$ ions to the Na1 and Na3 sites ensures complete HP2 gate opening via a conformational selection-like mechanism and enables high-affinity substrate binding via electrostatic attraction. The combination of Na$^+$-stabilized gate opening and electrostatic coupling of aspartate to Na$^+$ binding provides a constant Na$^+$:substrate transport stoichiometry over a broad range of neurotransmitter concentrations.

INTRODUCTION

Glutamate is the major excitatory neurotransmitter in the mammalian central nervous system. After its release from presynaptic nerve terminals, glutamate is effectively removed from the synaptic cleft by glial and neuronal excitatory amino acid transporters (EAATs), supporting fast and reliable glutamatergic synaptic neurotransmission. EAATs are trimeric secondary active glutamate transporters (1, 2), in which the three monomers function independently. One glutamate is cotransported with three Na$^+$ and one H$^+$ in exchange for one K$^+$ (3), and experimental evidence supports a constant 3:1 Na$^+$:substrate transport stoichiometry over a broad range of substrate concentrations in EAATs and Glt$_{Ph}$ (3–5). Coupling the transport of one glutamate to several ions permits glutamate uptake against up to 10^6-fold concentration gradients and contributes to maintaining low extracellular glutamate concentrations in the central nervous system (3, 5). EAATs are not only secondary active transporters but also Cl$^-$ channels (1, 2, 6, 7), and changes in Cl$^-$ channel function are responsible for movement disorder and epilepsy in certain forms of episodic ataxia (8–10).

X-ray crystallography of the prokaryotic homologs Glt$_{Ph}$ and Glt$_{Tk}$ revealed that glutamate transport is based on elevator-like conformational changes that move the transport domain with the bound substrate across the membrane (11, 12). Hairpin loop 2 (HP2) serves as a gate controlling access to the substrate-binding pocket in both the outward- and inward-facing states (13–16), and translocation of the transport domain is only possible with closed HP2 (14, 17). HP2-gating dynamics are allosterically regulated by ion and substrate binding (17–21). HP2 is tightly closed in fully bound or *apo* transporters (16, 17, 22, 23), whereas addition of the competitive transport blocker DL-*threo*-β-Benzyloxyaspartic acid (TBOA) resulted in crystallization of HP2 in the open state (16, 24). Closure of HP2 after the association of ions and/or substrates in certain combinations, but not in others, allows for stoichiometrically coupled substrate transport (18–21).

Elevator translocation—first found in Glt$_{Ph}$ (11)—is an intriguing alternating-access mechanism used by several secondary active transporters (25). Elevator transporters have two functionally specialized domains: a static scaffold domain (trimerization domain in EAATs/Glt$_X$) and a mobile transport domain, which accommodates the substrate- and ion-binding sites. Elevator translocation involves large-scale rigid-body motions of the transport domain against the scaffold domain, thereby moving the bound substrate from one side of the membrane to the other. The elevator alternating-access mechanism accounts for various functional properties of the EAATs and related homologs and permits combining high substrate selectivity with complex transport stoichiometries (25, 26). The separation between ion and substrate binding and translocation dynamics allows for the evolutionary adjustment of ion-coupling mechanisms without changing the binding sites or the translocation mechanism, resulting in a variety of transport stoichiometries in the SLC1 family—ranging from purely Na$^+$- or H$^+$-coupled transporters in prokaryotes to Na$^+$-, K$^+$-, and H$^+$-coupled eukaryotic glutamate transporters (EAATs) and Na$^+$-dependent neutral amino acid exchangers (ASCTs) (19). However, certain features of elevator transport might impair effective transport at fixed stoichiometry, and how these limitations are overcome remains unclear. In particular, specific mechanisms are required to lock the transporter in the inward or outward orientation after completing substrate translocation to prevent additional back-and-forth movements of the transport domain (27). To enable stoichiometric transport of the substrate together with multiple

[1]Institute of Biological Information Processing (IBI-1), Molekular- und Zellphysiologie, and JARA-HPC, Forschungszentrum Jülich, Jülich, Germany. [2]Institut de Biologie Structurale (IBS), Université Grenoble Alpes-CEA-CNRS, 38000 Grenoble, France. [3]Institute of Biological Information Processing (IBI-7), Structural Biochemistry, Forschungszentrum Jülich, Jülich, Germany. [4]Research Center for Molecular Mechanisms of Aging and Age-Related Diseases, Moscow Institute of Physics and Technology, Dolgoprudny, Russia. [5]Institute of Crystallography, RWTH Aachen University, Aachen, Germany. [6]JuStruct: Jülich Centre for Structural Biology, Forschungszentrum Jülich, Jülich, Germany. [7]Institute of Clinical Pharmacology, RWTH Aachen University, Aachen, Germany.
*These authors contributed equally to this work.
†These authors contributed equally to this work.
‡Corresponding author: Email: j.machtens@fz-juelich.de (J.-P.M.); c.fahlke@fz-juelich.de (C.F.)

ions, a strict binding order of the ions and substrate has to be enforced, and elevator translocation has to stall whenever the transport domain is incompletely occupied. Last, to permit coupled transport over a broad range of substrate concentrations (*3–5*), mechanisms need to exist to cooperatively accelerate ion and substrate binding to reach the fully bound configuration.

The coupling of Na^+ and substrate binding is crucial for effective transport by EAATs/Glt_X. Initially, two Na^+-binding sites, Na1 and Na2, were resolved in Glt_{Ph} crystal structures with the aid of thallium soaking (*16*). The Na1 site is coordinated by carbonyl oxygens of residues from transmembrane domains 7 and 8 (TM7 and TM8) located below the substrate-binding pocket and thus needs to be occupied before substrate binding, while the Na2 site is formed by the backbone of closed HP2 and TM7 and becomes occupied by the last Na^+ ion after substrate binding (*16*). The position of the third Na^+-binding site remained undefined for many years, and multiple sites have been proposed, some of which may serve as transient sites only (*17, 28–32*). However, a recent crystal structure of aspartate-bound Glt_{Tk} revealed the position of all three Na^+-binding sites, including the Na3 site, which has the highest Na^+ affinity among the three Na^+-binding sites (*23*).

To understand ion-coupling mechanisms in secondary active elevator glutamate transporters, we studied Na^+ association to substrate-free, outward-facing Glt_{Ph} and the mechanisms responsible for coupling Na^+ binding to HP2 dynamics and aspartate binding using a combination of molecular dynamics (MD) simulations, fluorescence spectroscopy, and x-ray crystallography. We demonstrate that its inherent flexibility causes HP2 to open after translocation, permitting Na^+ ions to reach the Na1- and Na3-binding sites. Occupation of both sites in turn stabilizes the open HP2 gate, thereby exposing the substrate-binding pocket to the extracellular space. Last, we demonstrated that electrostatic interactions represent an additional direct Na^+:substrate coupling mechanism that supports stoichiometrically coupled substrate transport.

RESULTS

HP2 gate opening precedes Na^+ binding

We performed unguided atomistic MD simulations of wild-type (WT) Glt_{Ph}, starting from the outward-facing, *apo* conformation with a closed HP2 gate (*17*) to simultaneously monitor Na^+ binding and dynamics of the extracellular gate HP2. On time scales of several microseconds, we observed multiple spontaneous opening and closing events (Fig. 1, A and B, fig. S1A, and table S3), in which the degree of HP2 opening was similar to that observed in the crystal structure of Glt_{Ph} bound to the competitive inhibitor TBOA (*16*). Thus, the HP2 gate is intrinsically flexible and can spontaneously switch between the open and closed states in the *apo* conformation.
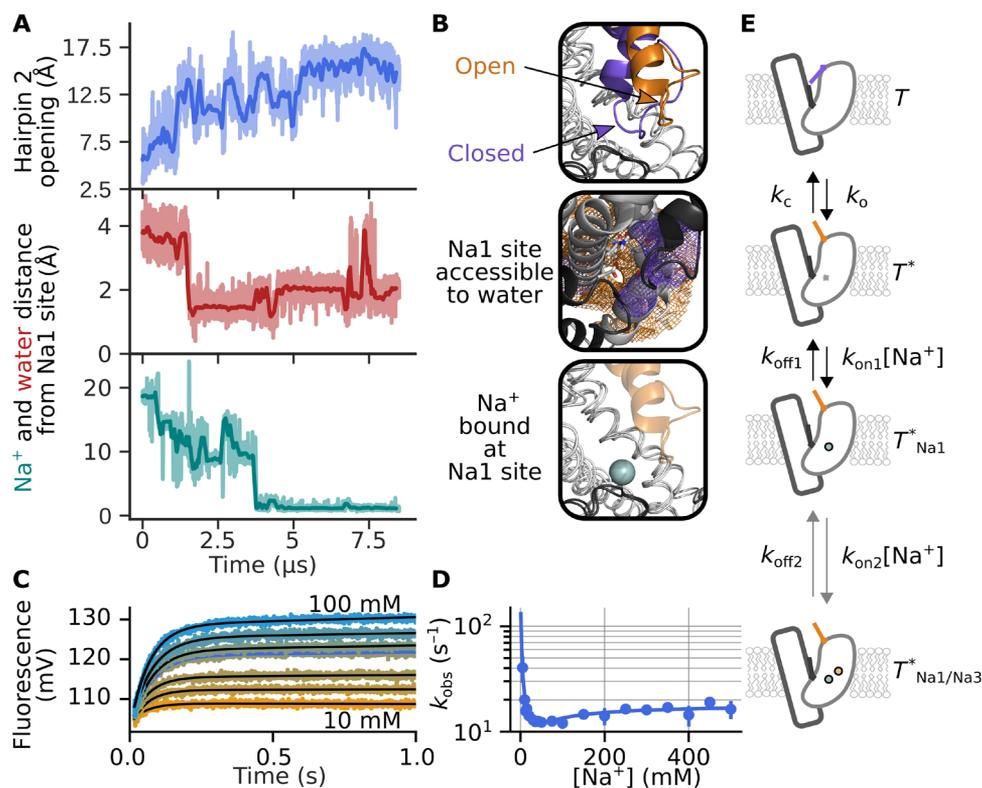
Fig. 1. Unguided MD simulations reveal Na^+ binding to the Na1 site upon HP2 gate opening. (**A**) Top: Time course of HP2 opening (measured as distance between S279 and G354 at the tips of HP1 and HP2, respectively). Middle: Distance of closest waters to the Na1 site. Bottom: Na^+ distance to the Na1 site in unguided MD simulations of trimeric Glt_{Ph} starting from the outward-facing, gate-closed, *apo* state (see also fig. S1A). (**B**) Top: Representative snapshots from the simulations in (A) with extreme positions of HP2. Middle: Water densities around the Na1 site shown as mesh contoured at 2σ (violet, closed HP2; orange, open HP2). Bottom: Na^+ bound to the Na^+ site at the end of the simulation. (**C**) Representative fluorescence responses to rapid Na^+ application to detergent-solubilized F273W Glt_{Ph} in stopped-flow experiments at 20°C. Black lines show monoexponential fits. (**D**) Observed rates (k_{obs}) of experiments performed as shown in (C) (*n* = 3 to 10 for each condition) and corresponding fits of the kinetic model in (**E**). (**E**) Four-state model of Na^+ binding to the *apo* transporter.

Spontaneous Na^+ binding to the Na1 site was reproducibly observed in 10 independent simulations (Fig. 1, A and B, fig. S1A, and table S3). Our simulations revealed a consistent pattern: HP2 opening was initially followed by hydration of the Na1 site and then by Na^+ binding to the Na1 site (Fig. 1, A and B, and fig. S1A). On the time scale of these simulations, we did not observe Na^+ binding to a second site and HP2 remained open after Na^+ association. Thus, our simulations demonstrated that Na^+ binding to the Na1 site follows Na^+-independent HP2 opening.

To further scrutinize the order of Na^+ binding and associated conformational changes, we used time-resolved stopped-flow fluorescence experiments in the F273W Glt_{Ph} mutant (Fig. 1, C and D), a reporter for Na^+ and aspartate binding with unimpaired WT transport kinetics (21). Rapid Na^+ application at different concentrations caused slow increases in fluorescence intensity over a monoexponential time course (Fig. 1C). The k_{obs} decreased with rising $[Na^+]$ up to ~50 mM and then rose to a plateau (Fig. 1D). In a previous study, Hänelt et al. (21) used a smaller range of $[Na^+]$ and observed an approximately linear concentration dependence in observed rates, with values approximately twofold smaller than those we observed at the same $[Na^+]$. These differences are likely due to the experimental conditions: We substituted Na^+ with choline$^+$, whereas the other study substituted Na^+ with K^+.

HP2 opening caused a strong reduction in water accessibility of the tryptophan side-chain in MD simulations of F273W Glt_{Ph} (fig. S1C), indicating that the W273 fluorescence directly reports on HP2 opening and closing (33). The initial decrease in k_{obs} demonstrates that at least one slow, Na^+-independent conformational change occurs before Na^+ binding, indicating that Na^+ association to apo Glt_{Ph} is characterized by a mechanism similar to the classical conformational selection (34). However, a simple three-state model with a Na^+-independent step followed by one Na^+-association event cannot explain the biphasic $[Na^+]$ dependence of k_{obs}, suggesting that at least one further Na^+-dependent binding process is involved. We therefore added a second Na^+-association step to the kinetic scheme and tested the resulting four-state model against our kinetic data: We modeled the first conformational change as HP2 gate opening, as suggested by our simulations, and the second and third steps as binding events at the two Na^+ sites (Fig. 1E). This model accurately described the Na^+ dependence of k_{obs} (Fig. 1D) and also predicted equilibrium fluorescence amplitudes that are close to the results of equilibrium titration experiments (fig. S1D). These results support the notion that Na^+ binds to Glt_{Ph} after adopting a preexisting open conformation for HP2, rather than directly inducing HP2 opening.

Occupation of the Na1 and Na3 sites stabilizes HP2 in the completely open state

To better understand the coupling between Na^+ binding and the HP2 gate, we determined the structure of WT Glt_{Ph} in the Na^+-bound conformation using the in meso approach to membrane protein crystallization (35). We obtained type 1 hexagonal crystals of P321 symmetry, with one protomer in the asymmetric unit that formed trimers within membrane-like two-dimensional (2D) crystals (fig. S2). The structure was solved to 2.5-Å resolution, revealing distinct electron densities at the Na1 and Na3 sites with coordination patterns indicative of Na^+ ions (Fig. 2, A and B). The densities overlapped with two of the three Na^+ sites identified in a recent crystal structure of Glt_{Tk} bound to one aspartate and three Na^+ ions with a similar coordination of the Na3 site by the backbone of Tyr^{89}
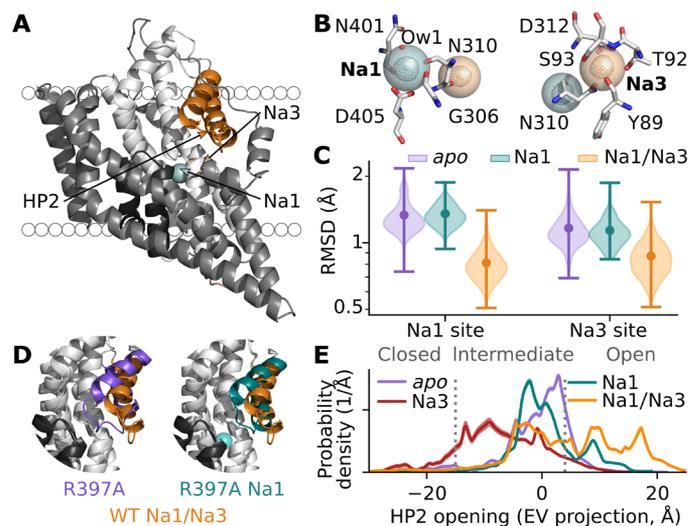
Fig. 2. Glt_{Ph} crystal structure reveals the Na1/Na3-bound fully open state. (A) X-ray crystal structure of Na^+-bound WT Glt_{Ph} at 2.5-Å resolution in the outward-facing conformation. (B) Close-up images of the occupied Na1 and Na3 sites (gray mesh, omit map contoured at 5.0σ) and the coordinating residues. (C) Root mean square deviation of binding-site residues from the crystal structure (A) in 60-ns MD simulations with either binding sites occupied or ions manually removed. (D) Superimposition of the Na^+-bound WT structure on apo [Protein Data Bank (PDB): 4OYE] or Na1-bound R397A Glt_{Ph} (PDB: 4OYF) to highlight differences in the HP2 gate. (E) Probability densities for HP2 opening as a function of Na1- and Na3-site occupancies from umbrella sampling simulations (EV, eigenvector).

and Thr^{93} and the side-chain oxygens of Val^{92} and Asp^{312} (23). To further confirm that the densities at the Na1 and Na3 sites correspond to Na^+ ions, we performed MD simulations of the structure with either both Na^+-binding sites occupied or with one or both ions manually removed. Root mean square deviation analysis of the side chains coordinating the Na^+-binding sites demonstrated that only simultaneous occupation of both sites ensures a conformational ensemble consistent with the crystal structure, confirming that our structure represents the Na1/Na3-bound state of WT Glt_{Ph} (Fig. 2C). In this conformation, HP2 is fully open, resembling the previously described structure of Glt_{Ph} bound to the competitive inhibitor TBOA (16). Our Na1/Na3-bound structure differs from the resolved crystal structure of Na1-bound R397A-Glt_{Ph} (17), in which only the tips of the HP2 gate are open (Fig. 2D). We will refer to this structure as the open conformation throughout the remainder of this work.

To quantify the energetics of HP2 opening as a function of different Na^+ occupancies, we used umbrella sampling simulations (fig. S3). We defined three discrete HP2 states according to our structural and functional observations: closed, intermediate, and open (fig. S4). In the apo state, we observed HP2 mostly in the intermediate conformation, with low occupation of the open state and a negligible occupation of the closed state (Fig. 2E). Occupation of the Na1 site increased the probability of the open state, while exclusive Na3 occupation shifted the distribution toward the closed state; however, since our simulations suggest that Na^+ ions bind to the Na1 site first, the Na3-only bound state probably has little physiological relevance and will not be considered further. When both the Na1 and Na3 sites were occupied, we observed a strong increase in the probability of the open state (Fig. 2E). We conclude that HP2-gate

opening in the Na$^+$-bound state is similar to the HP2 conformation found in the TBOA-bound structure and that occupation of both Na1 and Na3 sites is necessary to stabilize the open HP2 gate.

Distinct conformational changes precede and follow Na$^+$ binding

Comparison of *apo*, Na$^+$-bound, and fully bound crystal structures highlighted conformational differences in a series of residues in the transport domain around the binding sites that are likely coupled to Na$^+$ binding. Rearrangements of these residues may be involved in the slow cooperative binding of Na$^+$ ions to the Na1 and Na3 sites in the absence of aspartate (*20, 21, 36*), but it is unclear how these conformational changes in the binding pockets are coupled to HP2 dynamics and Na$^+$ binding. In multiple independent simulations, we measured inter-residue distances for residues around the ion-binding pockets (but not those in HP2) and labeled each trajectory frame according to water accessibility and Na$^+$ occupation of the Na1 and Na3 sites (*apo*, water-accessible/primed, Na1-bound, or Na1/Na3-bound). Input data were unbiased MD simulations initiated from the *apo* state (total simulation time: ~72 μs; table S3) with and without spontaneous HP2 opening and Na1 binding and from our Na1/Na3-bound structure (total simulation time: ~4.4 μs; table S3). We then trained a machine-learning model on labeled

inter-residue distances to assign functional states based on side-chain conformers around the ion-binding pockets only, i.e., without explicitly considering HP2 dynamics. A support vector machine (SVM) assigned these functional states based on residue distances with good accuracy (*apo*, 96.5%; primed, 95.1%; Na1-bound, 47.4%; Na1/Na3-bound, 100%; fig. S6).

To identify conformational transitions between the *apo*, water-accessible/primed, Na1-bound, and Na1/3-bound states, we compared the assumed inter-residue distances for the distinct functional states (Fig. 3A). We next selected those residue pairs that closely interact (minimum distance of <10 Å) and present a substantial distance-distribution change between states (overlap with *apo* distribution of <50%). This analysis revealed that only few residues (Y89, G306, N310, M311, D312, G313, T314, R397, T398, N401, and D405) move significantly during these rearrangements (Fig. 3, B and C). Spontaneous opening of HP2 is followed by breaking the bond between N401 and N310 and an upward movement of N401 within the glutamate transporter signature sequence, the NMDGT motif in TM7; this concerted movement increases water accessibility to the Na1-binding pocket. Binding of the first Na$^+$ ion induces the upward movement of R397. Next, the initial movement of M311, which frees up the Na3 site, is stabilized by a weak interaction between N401 and T314. Last, occupation of both the Na1 and
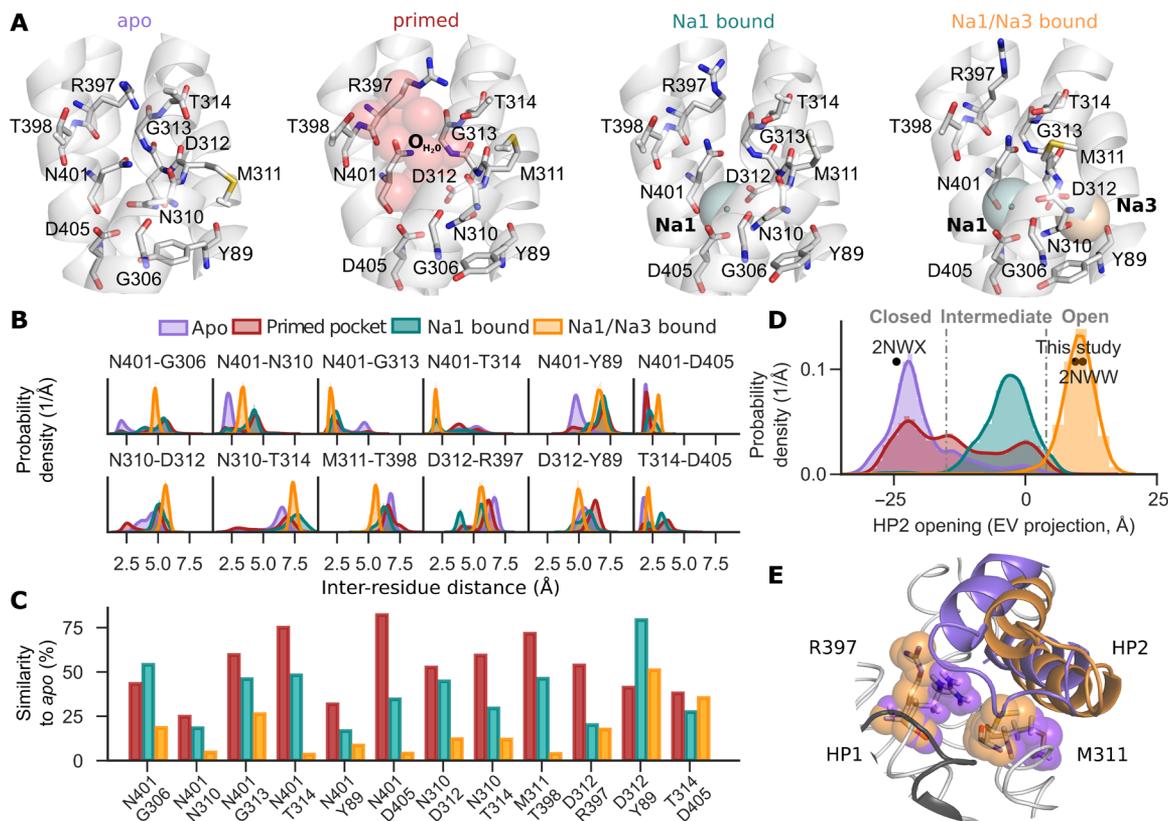
Fig. 3. Identification of residues in distinct Na$^+$-associated rearrangements in the binding pockets. (**A**) Close-up images of the substrate and ion-binding pockets in the *apo*, primed (hydrated), Na1-bound, and Na1/Na3-bound states. Residues involved in conformational rearrangements between states are shown as sticks. (**B**) Inter-residue distances in unguided MD simulations of all residues surrounding the Na1 and Na3 sites were classified into the four states shown in (A) using a SVM (see Materials and Methods). Selected distance distributions with the largest differences between assigned states are shown to identify key residues. (**C**) Overlap of normalized distance distributions in the different states with the *apo* state for the distance pairs in (B) identified residues involved in the conformational changes. (**D**) HP2-distance distributions assumed in the binding-pocket states as classified by the SVM analysis. (**E**) Depiction of HP2 in the closed and the open state, with M311 and R397 shown in the *apo* (violet) and Na$^+$-bound (orange) states.

Na3 sites locks the binding pocket in an aspartate-bound–like position: The R397 side chain moves further away from the binding pocket allowing N401 and T314 to form a hydrogen bond, while N310 is positioned between the two bound Na^+ ions and M311 flips upward to lock HP2 in the completely open state.

The conformational distribution of HP2 in unbiased MD simulations, analyzed separately for the assigned conformational states of the binding pocket by the SVM, is consistent with the Na^+ dependency of HP2 opening in our umbrella sampling simulations (Fig. 2E): While HP2 is closed in the *apo* state, occupation of the Na1 and Na3 sites causes a probability shift toward the completely open conformation of HP2, with intermediate degrees of opening being reached when only Na1 is occupied. In addition, this analysis reveals that the initial Na^+-independent priming step of the binding pocket is already associated with an increase in HP2 open probability (Fig. 3D). Thus, the observed Na^+ dependency of HP2 opening has its foundation in a tight thermodynamic coupling of HP2 with Na^+-dependent conformational changes of the transport domain. Some of the residues involved are highly conserved across the glutamate transporter family, corroborating their functional significance (e.g., N310, M311, D312, G313, T314, R397, and N401). The two bulky residues R397 and M311 assume characteristic positions as a function of Na^+ site occupancy and may thus represent key mediators of Na^+-dependent HP2 gating (Fig. 3E). We conclude that binding at both the Na1 and Na3 sites induces rearrangements of a few conserved residues in the binding pockets that stabilize the open HP2 conformation. Therefore, the mechanism responsible for cooperative Na^+ binding involves a series of discrete conformational changes, consistent with the experimentally supported four-state binding model.

Na1- and Na3-binding pathways only become accessible after HP2 opening

The Na1 and Na3 ion-binding sites were previously described using crystallography and free-energy calculations (23, 30, 37), but the ion-binding pathways remained unclear. In microsecond-long simulations of the *apo* state, we reproducibly observed spontaneous Na^+ binding from the extracellular side to the Na1 site, but not to the Na3 site (Fig. 1A and table S3). Given the slowness of Na^+ binding and associated conformational changes observed experimentally (20, 21), the inability of MD simulations to sample spontaneous Na^+ binding to Na3 is not surprising. We therefore studied the reverse process: Na^+ unbinding from the Na1/Na3-bound structure (Fig. 2, A and B). Since Na^+ ions remained stably bound at the Na1 and Na3 sites in unbiased MD simulations, we applied a weak, short-range, repulsive potential between the bound Na^+ ions and coordinating atoms to destabilize ion coordination at the Na^+ sites without imposing the direction of unbinding. In these simulations, we reproducibly observed Na^+ unbinding on simulation time scales of ~100 ns.

As expected, triggering the unbinding of the Na1 ion alone resulted in a pathway indistinguishable from spontaneous binding to this site in unbiased MD simulations. We then investigated Na^+ dissociation starting from the Na1/Na3-bound state by simultaneously destabilizing both ions bound at the Na1 and Na3 sites. Whereas the ion bound to Na1 dissociated along a pathway similar to that of spontaneous Na1 binding, we observed two distinct Na3 dissociation pathways depending on whether the ion at Na1 dissociated before or after the Na3 ion. When Na1 dissociated first, in about half of the simulations, Na^+ hopped from Na3 to the available Na1 site along a pathway below the unwound part of TM7, from which it eventually dissociated to the extracellular solution. In the presence of a bound ion at the Na1 site, the Na3 ion dissociated along a previously undiscovered pathway lined with hydrophobic residues located above the unwound part of TM7. The second pathway is lined by two methionine residues (M311 and M362), which undergo Na^+-dependent conformational changes (Fig. 4, A and B). The need to overcome these barriers (i.e., breaking the bonds formed in the transient occupation of the Na1 site or crossing a highly hydrophobic region) may explain the slowness of Na^+ binding at the Na3 site. While M311 is highly conserved across the glutamate transporter family, M362 is substituted by a threonine in EAATs and is partly responsible for differential substrate recognition among homologs (38, 39).

We conclude that Na^+ can access the Na3 site either through Na1, as previously suggested (30), or through a narrow hydrophobic pathway partially controlled by the position of M311. All Na1 and Na3 (un)binding pathways become accessible to Na^+ ions only after HP2 opening (Fig. 4C), providing further support for a conformational selection–like mechanism for Na^+ binding and HP2 opening.

Mutating key residues partially uncouples Na^+ binding from HP2 gating

Two of the important contributors to Na^+-associated conformational changes, M311 and R397 (Fig. 3, A to C and E), are conserved in EAATs, Glt_{Tk}, and Glt_{Ph}, and side-chain substitutions are reported to reduce the Na^+ dependence of substrate binding, emphasizing their importance in ion-substrate coupling (17, 40). To study their contribution to Na^+-dependent HP2 dynamics, we determined the probability distributions for HP2 opening for the *apo* and Na1/Na3-bound states of R397A and M311A Glt_{Ph} using umbrella sampling. Both mutants had an increased probability for the closed state of the gate in the *apo* transporter and for the intermediate state (but
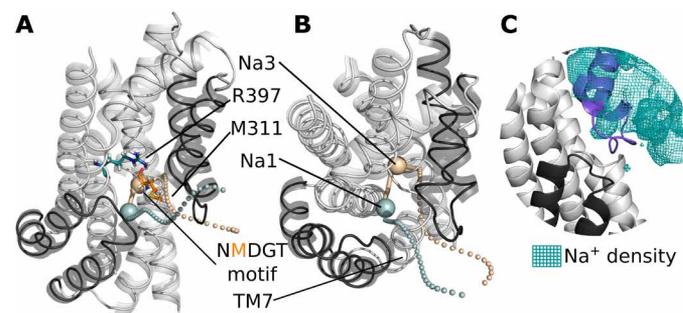
Fig. 4. Na^+-binding pathways in the *apo* state. (A and B) Side and top views of Na^+-binding pathways to the Na1 (teal) and Na3 (orange) sites, as obtained from unbinding simulations starting from the Na1/Na3-bound state. A weak flat-bottomed distance restraint of the bound Na^+ ions to the binding sites was used to induce unbinding on the 100-ns time scale. Na^+ ions can bind to Na3 either indirectly via the Na1 site below the NMDGT segment of TM7 or directly through a narrow hydrophobic pathway above TM7 gated by M311. R397 (teal) and M311 (orange) are shown as sticks. (C) Na^+ density (contoured at 0.2σ) obtained from multiple unbiased simulations of the outward-facing, *apo* state (Fig. 1), considering only trajectory parts with closed HP2, demonstrates that the Na1 and Na3 sites are not accessible when HP2 is closed.

not for the fully open state) in the Na$^+$-bound transporter (Fig. 5A). For R397A, these results are consistent with the observation that the Na1-bound crystal structure of R397A Glt$_{Ph}$ presents a smaller opening for HP2 (*17*) compared with the Na1/Na3-bound WT crystal structure (Fig. 2, A and D). Figure 5B provides differences between the cumulative probabilities of HP2 being open in the presence and absence of Na$^+$ for WT and mutant Glt$_{Ph}$. The fully open state is required to permit aspartate binding (fig. S4) and coincides with the open state resolved in the Na1/Na3-bound crystal structure. In the WT, Na$^+$ binding to Na1 and Na3 markedly increased the probability of the fully open state of HP2; however, in both mutants, the highest probability was seen for the intermediate state of HP2, which reduced the overall probability for the open state (Fig. 5B and fig. S7, A to C).

We next studied the kinetics of R397A and M311A in stopped-flow fluorescence experiments. For F273W Glt$_{Ph}$ and for F273W-M311A Glt$_{Ph}$, Na$^+$ application increased, and aspartate application decreased tryptophan fluorescence amplitudes; R397A caused an inversion of fluorescence responses (fig. S7, D to F). This inversion is due to R397A-induced changes in water accessibility of W273: HP2 opening increases water accessibility in F273W-R397A Glt$_{Ph}$ but reduces accessibility in the other mutants (fig. S1C). Thus, the Na$^+$- and aspartate induced changes in F273W fluorescence report on HP2 dynamics in all tested transporters. The observed rate (k_{obs}) of Na$^+$-induced fluorescence changes of F273W-R397A Glt$_{Ph}$ displayed monophasic dependence on [Na$^+$] (Fig. 5C). Fitting the four-state model against k_{obs} as a function of [Na$^+$] revealed that in R397A, the HP2 gate has an increased opening rate and a decreased closing rate and that the on-rate of the first Na$^+$-binding step is increased, while the second Na$^+$-binding step seems to be uncoupled (Fig. 5C and table S2). In M311A, the HP2 opening rate is increased and the closure rate is decreased, while both the first and second binding rates are faster, thus increasing the apparent affinity for Na$^+$ and markedly speeding up the observed rates (Fig. 5C and table S2). We

conclude that the altered kinetics of Na$^+$ binding in M311A and R397A mutants are mediated indirectly by modifying HP2 opening and directly by modifying the rate constants associated with the Na$^+$ binding.

Na$^+$ binding promotes aspartate association by electrostatic attraction

Opening of HP2 before Na$^+$ binding could permit substrate association even without prior Na$^+$ association and thus cause a reduction in the Na$^+$:substrate coupling ratio at high substrate concentrations. However, experimental evidence supports a strict thermodynamic coupling of substrate binding to [Na$^+$] (*36*) with a 3:1 Na$^+$:substrate transport stoichiometry at various substrate concentrations in EAATs and Glt$_{Ph}$ (*3–5*). Na$^+$ ions are not directly involved in substrate coordination (*16*, *23*), and we therefore assumed that Na$^+$ binding facilitates aspartate binding via long-range electrostatic attraction.

To test this hypothesis, we conducted multi-microsecond-long, unguided aspartate-binding simulations at [NaCl] ≈ 200 mM and [Asp$^-$] ≈ 10 mM (table S3). Starting from the Na1/Na3-bound crystal structure with the open HP2 conformation (Fig. 2A), we reproducibly observed aspartate association and dissociation with the open transport domain (table S3). The maximal aspartate density overlapped with the aspartate molecule in the crystal structure of fully bound Glt$_{Ph}$ (Fig. 6A) (*16*). Further inspection of the simulated aspartate densities revealed an additional intermediate aspartate-binding site (Fig. 6B), which overlapped with a phosphate ion that cocrystallized in our Na$^+$-bound structure, suggesting that this initial association site for aspartate attracts anions and that the phosphate ion can mimic the aspartate carboxyl group (Fig. 6C and fig. S5). The comparison of aspartate distributions for different occupancies of the Na1 and Na3 sites revealed negligible aspartate binding to *apo* and Na1-bound Glt$_{Ph}$, and a strong increase in aspartate densities near the aspartate-binding site upon Na$^+$ occupation of both Na1 and Na3 (Fig. 6B). We conclude that aspartate association with
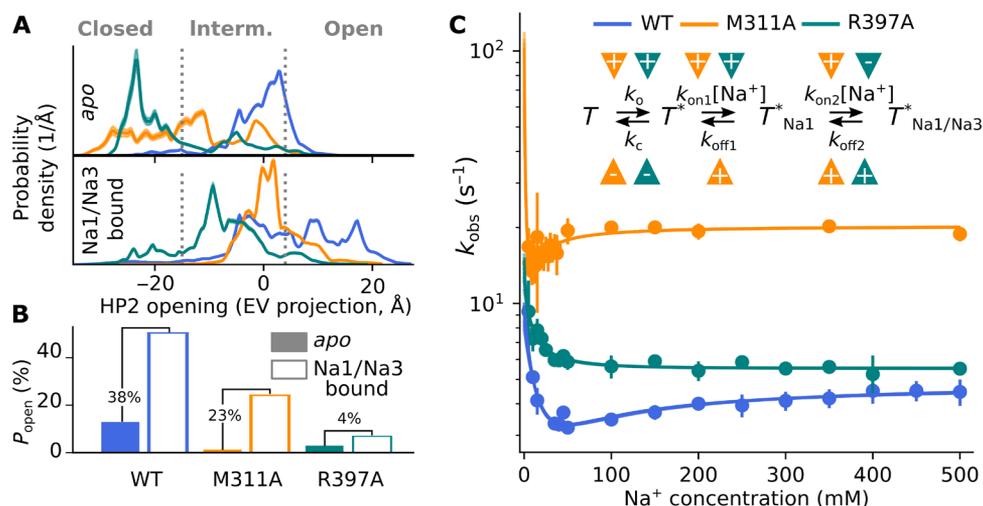
Fig. 5. Mutation of key residues uncouples Na$^+$ binding from gate opening. (**A**) Probability densities for HP2 opening in the *apo* or Na1/Na3-bound state for WT (Fig. 2E) and mutant Glt$_{Ph}$ from umbrella sampling simulations (WT, blue; M311A, yellow; R397A, green). (**B**) Integrated probabilities for the fully open state in the *apo* or Na1/Na3-bound state from probability distributions in (A). Numbers indicate the increase in absolute probability upon Na$^+$ binding to the Na1 and Na3 sites. (**C**) Kinetics of rapid Na$^+$ application to detergent-solubilized Glt$_{Ph}$ in stopped-flow fluorescence experiments at 10°C (F273W, blue; F273W-M311A, yellow; F273W-R397A, green; n = 3 to 7 for each condition). M311A and R397A accelerate the observed kinetics and modify the Na$^+$ dependence of k_{obs} (inset, four-state model used to fit the data with arrowheads indicating the change in rate induced by the mutants; see also table S2).
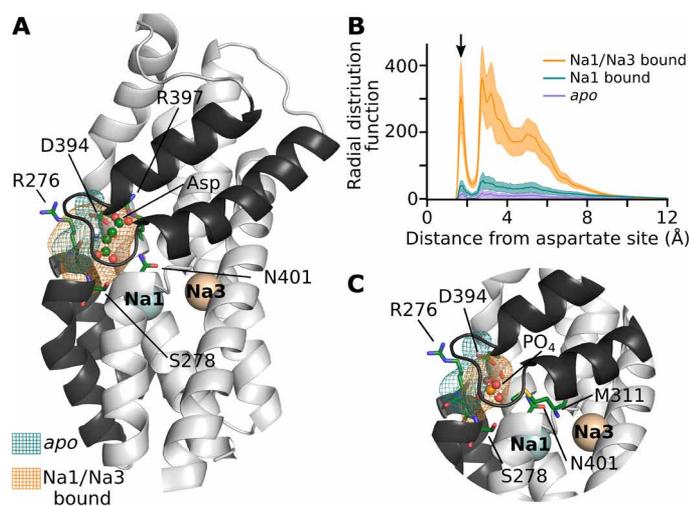
Fig. 6. Electrostatic Na⁺:substrate coupling. (**A**) Averaged aspartate densities are shown as isodensity meshes contoured at 0.2σ from unguided MD simulations of trimeric, Na1/Na3-bound, substrate-free, gate-open Glt$_{Ph}$ with either the Na1 and Na3 sites occupied (orange) or Na⁺ manually removed (cyan) from the sites (bulk [NaCl], 200 mM; [Asp], 10 mM). The bound aspartate in the Na⁺/aspartate-bound crystal structure (PDB: 2NWX) is shown as sticks and balls. (**B**) Radial distribution function of aspartate molecules to the center of the binding pocket in unguided MD simulations as in (A); the arrow indicates the density peak corresponding to the crystallographically resolved aspartate-binding site. (**C**) Bound phosphate in the Na1/Na3-bound crystal structure overlaps with aspartate density (contoured at 2σ) in simulations and reveals an intermediate binding site. Coordinating residues of the phosphate are shown as sticks.

Glt$_{Ph}$ in the HP2 open state is mediated by Na⁺-dependent electrostatic interactions, constituting a second direct Na⁺:substrate coupling mechanism.

DISCUSSION

The stoichiometrically coupled cotransport of three Na⁺ ions drives substrate transport in Glt$_{Ph}$ and mammalian EAATs (*3, 4*). Because none of the three Na⁺ ions directly interacts with the bound substrate, allosteric interactions are required for sodium-substrate coupling (*26*). It is well established that at least one Na⁺ ion binds after aspartate association to the Na2 site (*16, 36*), strengthening aspartate binding by locking HP2 in a closed state (*16*) and preventing dissociation (*41*). Na⁺ binding to the *apo* transporter is necessary for fast aspartate association (*20, 41*); however, the number of Na⁺ ions involved in the different steps of this process, the order of associated conformational changes, and the mechanisms for coupling to aspartate binding have remained unclear. Here, we used atomistic MD simulations, fluorescence spectroscopy, and x-ray crystallography to characterize Na⁺ binding to *apo* Glt$_{Ph}$. MD simulations showed that Na⁺ binding requires prior opening of the HP2 gate and maturation of the ion-binding pockets, thus explaining the intrinsic slowness of Na⁺ binding to *apo* Glt$_{Ph}$ (*21*). Moreover, we found that HP2 is intrinsically flexible, permitting *apo* Glt$_{Ph}$ to adopt the open HP2 conformation for a considerable fraction of time. In unbiased simulations, Na⁺ binding occurred after HP2 opening (Fig. 1A and fig. S1A). We verified the order of HP2 opening and Na⁺ binding in kinetic experiments, which revealed a decrease in k_{obs} at low [Na⁺], reminiscent of a conformational selection binding mechanism (Fig. 1E). However, the biphasic behavior of k_{obs} at increasing [Na⁺] demon-

strates that the process cannot be simply reduced to this mechanism but must be described by a more complex four-state model, in which HP2 opening is followed by two Na⁺-binding events. Free-energy calculations demonstrated that Na⁺ binding to the Na1 and Na3 sites causes a population shift toward the open state of HP2, with concomitant occupation of Na1 and Na3 required for maximal HP2 opening (Fig. 2E).

We solved the structure of Na⁺-bound WT Glt$_{Ph}$ at 2.5-Å resolution (the highest resolution reported for any SLC1 transporter) and found HP2 in a fully open conformation, resembling its position when TBOA is bound (*16*). A phosphate ion was cocrystallized at a site predicted to partially overlap with an additional intermediate aspartate-binding site in aspartate binding simulations (Fig. 6C and fig. S5A), suggesting that this initial association site for aspartate attracts anions and that the phosphate can mimic the aspartate carboxyl group. However, competition experiments failed to show a significant change in aspartate-binding affinity in the presence of phosphate (fig. S5B). MD simulations starting from the resolved Na1/Na3-bound structure, including the bound phosphate molecule, revealed significant deviations of the Na⁺ ions from the crystal structure. In contrast, all simulations with the phosphate ion manually removed perfectly reproduced the positions of Na⁺ ions at both sites in the crystal structure, suggesting that the observed phosphate-binding site has rather low occupancy in the crystal (fig. S5C). Moreover, crystallographic B-factors of the phosphate are much higher than those of the protein or the Na⁺ ions (table S1). Furthermore, calculation of the overlap between HP2 at different degrees of opening in our simulations and the density of bound phosphate demonstrated that phosphate—unlike TBOA—does not prevent HP2 closure through steric hindrance (fig. S5D). Thus, the large degree of HP2 opening observed in the crystal structure is not caused by the presence of the bound phosphate. It rather represents the physiological Na⁺-only-bound state, which we reproduced by long time-scale MD simulations starting from the HP2-closed state (Fig. 1, fig. S1A, and table S3). Electron densities at positions close to the Na1 and Na3 sites are consistent with earlier computational predictions (*30*) and the fully bound Glt$_{Tk}$ crystal structure (*23*); structural stability analysis using MD simulations confirms the assignment of Na⁺ ions instead of water molecules to these sites (Fig. 2C). Our newly resolved X-ray structure thus enabled us to determine which of the three Na⁺-binding sites are occupied before aspartate association. We used this structure for MD simulations and could demonstrate that occupation of both Na1 and Na3 is necessary to stabilize HP2 in its fully open conformation (Fig. 2E).

The only information previously available on the Na⁺-only-bound state was based on a crystal structure of outward-facing R397A Glt$_{Ph}$ at 3.4-Å resolution (which permitted assignment of only one Na⁺ at the Na1 site using thallium soaking) (*17*) and a cryogenic electron microscopy (cryo-EM) structure of inward-facing Glt$_{Tk}$ at 3.2-Å resolution in lipid nanodiscs (*14*). Because R397A reduces the substrate-binding affinity, alters substrate selectivity (*16, 42*), and disrupts thermodynamic coupling between Na⁺ and substrate binding (*40*), this Glt$_{Ph}$ structure is not expected to reflect the Na⁺-induced conformational changes in the native transporter. The degree of HP2 opening in R397A Glt$_{Ph}$ corresponds to the intermediate open state occupied in the presence of only Na1 in our simulations. In the cryo-EM structure of inward Glt$_{Tk}$, the residues around the Na1 and Na3 sites assumed a similar conformation as in our Na1/Na3-bound Glt$_{Ph}$ and the fully bound Glt$_{Tk}$ structures

(23), with HP2 exhibiting an intermediate degree of opening (compared with HP2 in the outward-facing state), thereby exposing the substrate-binding site to the intracellular solution (14). These results suggest that the identified Na$^+$-stabilized HP2 opening mechanism also applies to HP2 gating in the inward-facing conformation.

We used the newly resolved high-resolution structure of Na$^+$-only-bound WT Glt$_{Ph}$ to identify Na1- and Na3-binding pathways through unguided simulations of Na$^+$ binding and unbinding (Fig. 4). In the *apo* transporter, one Na$^+$ ion associates with the Na1 site, followed by slower binding of a second Na$^+$ to the Na3 site. From simulated Na$^+$ dissociation from the Na3 site, we could infer two Na3-binding pathways: (i) Initial Na$^+$ association occurs at the Na1 site, followed by transition of the bound ion to an intermediate site [similar to the previously described site coordinated by D312 and residues from the Na1 site (29, 37)] before reaching the final Na3 site (23, 30) or (ii) direct binding through a narrow hydrophobic pathway lined by two methionine residues (M311 and M362), which becomes accessible upon HP2 opening. M311 is highly conserved across the EAAT family, while a conserved threonine present at residue 362 in all mammalian homologs is involved in substrate selectivity (38, 39). The temporal sequence of initial Na1 binding, which partially stabilizes the open HP2 conformation and facilitates Na3 association to maximize HP2 opening, optimizes Na$^+$ association.

Na$^+$ ions bind after HP2 opening and allosterically stabilize the open state (Figs. 1E, 2E, and 3D), indicating a mechanism for Na$^+$ binding more similar to conformational selection than to the induced-fit mechanism previously proposed for Na$^+$–HP2 coupling (43). In fluorescence spectroscopy experiments with V355W-S279PheCN Glt$_{Ph}$ (containing site-specific substitutions with one tryptophan and the unnatural amino acid 4-cyano-phenylalanine), Riederer and Valiyaveetil observed rates of Na$^+$-induced fluorescence changes that were more than 400-fold lower than in our experiments and increased with [Na$^+$] in a saturable manner. The slow kinetics were likely caused by the introduction of a bulky unnatural amino acid that impairs transport activity to less than 10% and strongly decreased Na$^+$ affinity, thus limiting an understanding of allosteric regulation by Na$^+$. The observed saturating [Na$^+$] dependence of apparent rates does not exclude our model of conformational selection-like Na$^+$ binding: Depending on the relative magnitude of the rates for different steps, a three-state model characterized by conformational selection can account for both concentration-dependent increases and decreases in observed rates (34). Using a tryptophan insertion mutant, F273W Glt$_{Ph}$, which has WT transport rates (21), we found that the apparent rates of Na$^+$-induced fluorescence changes exhibit a biphasic [Na$^+$] dependence. Biphasic [Na$^+$] dependence requires a four-state model as the most parsimonious linear model, in which the conformational change precedes the two binding events. In addition to these experimental results, our simulations demonstrate that the Na1 and Na3 sites are not accessible when HP2 is closed (Fig. 4C); in contrast, a key requirement for an induced-fit mechanism would be that the Na1 and Na3 sites are accessible when HP2 is closed. Consistent with a conformational selection-like mechanism, our simulations demonstrate the intrinsic flexibility of the external gate HP2, which can spontaneously open and close in the absence of bound Na$^+$ (Fig. 1A and fig. S1, A and B).

Because HP2 opening, which confers access to the aspartate-binding pocket, precedes Na$^+$ binding, the substrate might also be able to associate with the transporter in the absence of bound Na$^+$, resulting in a disturbed transport stoichiometry. However, our sim-

ulations demonstrate that substrate binding is negligible when HP2 is open in the absence of Na$^+$ and requires Coulomb attraction by the two Na$^+$ ions bound at the Na1 and Na3 sites (Fig. 6). Coupling between the two processes is ensured by the presence of bulky residues whose orientation favors the open or the closed state of HP2 and is under the control of Na$^+$ itself. By mutating two of these residues (R397 and M311) to alanine, we effectively decoupled Na$^+$ binding from aspartate association, revealing their central role in controlling HP2 conformation. HP2 dynamics differ in Glt$_{Ph}$ and EAAT1: Whereas HP2 is mostly open in *apo* EAAT1, it can close in *apo* Glt$_{Ph}$, permitting retranslocation and the K$^+$-independent transport of Glt$_{Ph}$ (19). The distinct HP2 dynamics of Glt$_{Ph}$ and EAAT1 also have important implications for Na$^+$ binding. Because Na$^+$ binds after HP2 opening, the altered HP2 dynamics will enhance Na$^+$ binding to the EAATs and may contribute to the faster transport kinetics of mammalian transporters.

Earlier kinetic models that described the EAAT transport cycle link substrate- and ion-binding steps and consider outward-inward isomerization as the only conformational change of the transporter (44, 45), without explicit representation of HP2-gating dynamics. Such models consistently predicted Na$^+$-binding steps before and after substrate binding. In particular, the work from Larsson and colleagues (45) demonstrated that Na$^+$ association before glutamate binding is associated with voltage-dependent conformational changes near HP2 in EAAT3, in agreement with the notion that the Na$^+$-associated HP2 dynamics (Fig. 2) are conserved across the EAAT family.

Neuronal and glial glutamate uptake needs to be concentrative, efficient, and robust against variations in physiological changes in ion and substrate concentration. The elevator mechanism ensures stoichiometrically coupled transport by permitting translocation of the transport domain only with certain ion and substrate occupations, i.e., in the fully bound configuration (including three Na$^+$ ions and the substrate), in the *apo* (in Glt$_X$ only), or in the K$^+$-bound configuration (in EAATs). During glutamate uptake, inward translocation is made possible via induced-fit substrate binding and HP2 closure (20, 21), while K$^+$ binding stabilizes HP2 in its closed conformation to enable K$^+$-bound retranslocation of the EAATs (19). To make elevator transport effective, unproductive back-and-forth movements of the transport domain need to be prevented. Our results explain observations in single-molecule fluorescence resonance energy transfer experiments, in which Glt$_{Ph}$ translocation undergoes transitions between dynamic and quiescent periods (27, 46) and propose a mechanism to prevent unproductive translocation dynamics. We demonstrate that the high flexibility of HP2 permits rapid opening that locks the transport domain into the outward-facing conformation after completing the translocation. Subsequent Na$^+$ binding increases the exposure time of the binding pocket to the extracellular solution by locking HP2 into the open state while at the same time attracting aspartate molecules via electrostatic interactions. Our results illustrate how the intrinsic flexibility of HP2 controls Na$^+$:substrate coupling to ensure Na$^+$-driven, concentrative glutamate uptake in the brain.

MATERIALS AND METHODS
MD simulations
MD simulations were performed using GROMACS 5.1 (47) with the AMBER99SB-ILDN force field and Joung parameters for the

ions, together with the SPC/E water model and Berger lipids, as previously described (7). Simulations of free aspartate binding (MD_Asp1–6; table S3 and Fig. 6) were performed using the CHARMM36m force field with the TIP3P water model using GROMACS 2018. All amino acids were modeled in their default ionization state to reflect the most probable state at neutral pH based on pK_a (where Ka is the acid dissociation constant) calculations using PROPKA. Protein structures were obtained from the Protein Data Bank (PDB) data bank [R397A Glt$_{Ph}$ apo, PDB: 4OYE; R397A Na1-bound, PDB: 4OYF; Na1/Na2/Asp-bound, PDB: 2NWX; Na1/TBOA-bound, PDB: 2NWW], and ligand occupation was modified as described in the text. Missing residues and mutations were modeled or reverted according to WT Glt$_{Ph}$ using MODELLER. The phosphate was modeled as dihydrogen phosphate to reflect the dominant protonation state at neutral pH using the parameters developed by Kashefolgheta et al. (48). However, unless otherwise stated, the co-crystallized phosphate was removed before setting up the simulations.

Simulations were performed on trimers in a cubic periodic box of dimensions ~140 × 140 × 110 to the power of 3, which was chosen to ensure a minimum distance between periodic copies of at least 40 Å. The simulation temperature was 310.15 K.

The transporter was embedded into a palmitoyl-oleoyl phosphaditylcholine (POPC) lipid membrane using g_membed (49); the position for embedding was obtained from the Orientations of Proteins in Membranes database. The protein/membrane system was surrounded by a ~400 mM solution of Na$^+$ and Cl$^-$ ions.

Equilibration consisted of three steps using the velocity-rescale thermostat and Berendsen pressure coupling: The first step was a 4-ns run with positional restraints on lipids in the z direction and position restraints on the protein heavy atoms and allowed for the bulk solution and lipid bilayer to equilibrate around the protein; in the second step (~800 ns), restraints were removed from the lipids and maintained on the protein to enable relaxation of lipids near the protein-lipid interface; and last, the system was equilibrated for 4 ns using backbone-only position restraints to enable side chains to equilibrate and obtain the velocities used in the following production runs. Production MD simulations used Parrinello-Rahman pressure coupling.

To accelerate Na$^+$ dissociation from the Na1/Na3-bound Glt$_{Ph}$ structure, a flat-bottomed distance restraint with a force constant 30,000 kJ mol^{-1} nm^{-2} (truncated after 0.3 nm) was used. Using these parameters, Na$^+$ dissociation from the Na1 and Na3 sites occurred over an average period of ~100 ns (Fig. 4).

Aspartate-binding simulations were performed by adding the substrate molecule randomly to bulk solution at a minimum distance of 15 Å from the substrate-binding pocket (Fig. 6).

To prevent spontaneous unbinding of dihydrogen phosphate and assess its effect on the Na$^+$ ions, the phosphate ion was restrained to its crystallographic position with an harmonic distance-restraint potential of 1000 kJ mol^{-1} nm^{-2} truncated at 3 Å from the center of mass of the backbone atoms of residues 278, 398, and 401 (fig. S5C).

Umbrella sampling simulations
We used principal components analysis (PCA) on a concatenated, monomeric trajectory, containing multiple free MD simulations, with spontaneous HP2 opening observed during the MD simulations. To reduce the noise due to motions unrelated to HP2 dynamics, we concentrated on a subset of atoms for PCA: the backbone

atoms of the transport domain. The biasing coordinate chosen for free-energy calculation was the first eigenvector obtained by the PCA analysis.

To obtain the conformations of interest, we then used essential dynamics (ED) sampling (50) to enforce a constant progression over time along the chosen coordinate. ED was carried out at a slow rate (time for change in HP2 conformation between closed and completely open: ~1.5 μs) to ensure the minimum possible bias on the simulation system. Next, a number of equally spaced snapshots (one snapshot every 2 Å, for the number of windows in each condition, see table S3) were extracted from the ED trajectories to start umbrella windows.

We used conformational flooding as implemented in GROMACS (47) to impose the bias along the PCA eigenvector in each umbrella window. A harmonic potential was applied to each window of interest, at the same position as determined by the snapshots obtained from ED. The potential was applied in two equilibration steps to minimize bias: In the first run, a potential with a force constant of 1000 kJ mol^{-1} nm^{-2} was applied for 10 ns with the Berendsen barostat, and the final conformation was used to start the production run, with a force constant of 1000 kJ mol^{-1} nm^{-2} with the Parrinello-Rahman barostat, from which the first 35 ns was discarded as equilibration. We applied the weighted histogram analysis method (51) to unbias and combine the probabilities obtained. To ensure convergence, the lengths of the production simulations were determined from the time-dependent overlap of unbiased probability distributions for the complete dataset with those obtained for non-overlapping 10-ns blocks (fig. S3; WT apo, 195 ns; WT Na1, 175 ns; WT Na3, 235 ns; WT Na1/Na3, 115 ns; M311A apo, 195 ns; M311A Na1/Na3, 115 ns; R397A apo, 175 ns; R397A Na1/Na3, 175 ns). Statistical errors were calculated with the Bayesian bootstrap method using 100 bootstrap samples.

Assignment of different HP2-gating states
The degree of HP2 opening (calculated as the distance between S279 on HP1 and G354 on HP2) assumes three states that correspond to the distance observed in different crystal structures (fig. S1B). To discretize this distance and the correlated eigenvector projection, we plotted the 2D kernel density estimate and chose appropriate thresholds to include the local maxima observed in the densities (fig. S4A). We then calculated the water and aspartate accessibility of the ion- and substrate-binding pockets in each assigned state. We used trj_cavity (52) to dynamically detect the water-accessible pocket and count the number of solvent molecules overlapping with the cavity in all umbrella sampling trajectories of WT Glt$_{Ph}$ in the apo state. Last, we calculated and plotted the average accessibility per window. To estimate aspartate accessibilities to the binding pocket, we calculated the averaged aspartate densities from free MD simulations with spontaneous aspartate binding to Na1/Na3-bound Glt$_{Ph}$ with open HP2 using GROmaρs (Fig. 6) (53). Subsequently, we calculated the HP2 densities in each umbrella sampling window using the aspartate density as a mask. Last, we estimated the overlap between HP2 and aspartate using the correlation between the two maps [where ρ$_{HP2}$(j) and ρ$_{asp}$(j) are the HP2 and the aspartate densities at position j, respectively, and μ$_{HP2}$ and μ$_{asp}$ are the spatial means]

$$\frac{\Sigma_j^n \left[(\rho_{HP2}(j) - \mu_{HP2}) \cdot (\rho_{asp}(j) - \mu_{asp}) \right]^2}{\Sigma_j^n (\rho_{asp}(j) - \mu_{asp})^2}$$

Similarly, we generated densities for bound ligands (bound aspartate, TBOA, and phosphate) from our newly resolved and previously published crystal structures (PDB: 2NWX and 2NWW) and calculated the overlap using these densities as reference densities (fig. S5B).

Classification of inter-residue distances using a SVM

We selected all residues within 10 Å of the Na1 and Na3 sites, while excluding all residues within 3 Å from the POPC bilayer and obtained a total of 43 residues. These did not include any residues from HP2. We used several microsecond-long free MD simulations starting from the *apo* structure (PDB: 4OYE; aggregate simulation time of ~50 μs, counting each protomer of the trimeric protein individually) and our Na1/Na3-bound structure (~4.4 μs) to calculate all inter-residue distances as the minimum distance. Each trajectory frame was labeled *apo*, primed, Na1-bound, or Na1/Na3-bound according to the water and Na$^+$ occupation status of the Na$^+$-binding sites, measured as the oxygen or Na$^+$ distance to the center of mass of the Na$^+$-coordinating protein atoms in the two Na$^+$ sites. For this, we used the following state definitions: *apo*: water distance, >2.5 Å; Na$^+$ distance from Na1, >5 Å; Na$^+$ distance from Na3, >2 Å; primed: water distance, <2.5 Å; Na$^+$ distance from Na1, >5 Å; Na$^+$ distance from Na3, >2 Å; Na1-bound: water distance, <2.5 Å; Na$^+$ distance from Na1, <5 Å; Na$^+$ distance from Na3, >2 Å; Na1/Na3-bound: water distance, <2.5 Å; Na$^+$ distance from Na1, <5 Å; Na$^+$ distance from Na3, <2 Å. We then trained a SVM with the radial basis function kernel using the scikit-learn python library (https://scikit-learn.org) to learn these state annotations based on the inter-residue distances. The accuracy was calculated as the number of correct predictions per state divided by the total predictions per independent simulation (*apo*: 96.7 ± 10.25%; primed: 76.8 ± 33.1%; Na1-bound: 53.18 ± 42.33%; Na1/Na3-bound: 100%; see fig. S6). Normalized distance histograms (calculated for each annotated state according to the SVM classification) were selected according to their distribution mean with selected distances having a mean of ≤5 Å in at least one of the four states; last, we measured the overlap to the *apo* distribution and presented significantly different distance pairs with a distribution overlap of <50% (Fig. 3).

Protein expression and purification

Mutant constructs were generated using polymerase chain reaction–based mutagenesis and verified by DNA sequencing.

Expression was performed in *Escherichia coli* Top10F, and the induction was performed with 0.1% L-arabinose at an optical density of 2.5. Proteins were purified by HIS-tag nickel-nitrilotriacetic acid (Ni-NTA) affinity gel and size exclusion chromatography in a buffer containing 200 mM NaCl, 20 mM Tris, and 1 mM n-dodecyl β-D-maltoside (DDM) at pH 7.4. Proteins were stored at −80°C for any measurement carried out more than a few hours after purification. For Na$^+$-free experiments, three rounds of buffer exchange in disposable salt exchange columns were performed in 200 mM ChCl, 20 mM tris, 1 mM DDM at pH 7.4.

Fluorescence measurements and analysis

Stopped-flow fluorescence recordings were performed using a μSFM (BioLogic Science Instruments), with excitation set at 297 nm, and emission filtered through a long-pass filter at 306 nm. Experiments were performed at 10° or 20°C. The dead time was calculated using the NATA (N-Acetyltryptophanamide)–NBS (N-bromosuccinimide) reaction as 6 ms for our experimental conditions. Time courses

were fitted with a monoexponential function with a global fitting using a least squares algorithm. The obtained observed rates were then fitted to a four-state model using distributed evolutionary algorithms in Python to run a genetic algorithm for 5000 generations. We repeated the fitting 10 times and showed the mean and SD.

Protein crystallization

Crystals were grown using an in meso approach (*54*), similar to that used in our previous work (*55*). Solubilized protein in the crystallization buffer was mixed with premelted (at 42°C) monoolein (Nu-Chek Prep) to form a lipidic mesophase. Aliquots (150 nl) of a protein-mesophase mixture were spotted onto a 96-well left circularly polarized glass sandwich plate (Paul Marienfeld) and overlaid with 400 nl of precipitant solution using the NT8 crystallization robot (Formulatrix). The best Glt$_{Ph}$ crystals were obtained with protein at a concentration of 20 mg/ml in 1 M KH$_2$PO$_4$/Na$_2$HPO$_4$, (pH 5.2). The crystals were grown at 22°C and reached the final size (100 to 150 μm) within 3 to 4 months and were hexagonal. Before harvesting, the crystals were incubated for 5 min in cryoprotectant solution [1.6 M KH$_2$PO$_4$/Na$_2$HPO$_4$ (pH 5.2) and 15% (w/v) glycerol]. All crystals were harvested using micromounts (MiTeGen), flash-cooled, and stored in liquid nitrogen.

Collection and treatment of diffraction data

X-ray diffraction data for native and mutant protein were collected at ID23-1 European Synchrotron Radiation Facility at 100 K with a PILATUS 6M detector (Dectris). Diffraction images were processed with XDS program package (*56*). Aimless from CCP4 suite (*57*) was used for symmetry determination, scaling and merging data, and to convert intensities to structure factor amplitudes and generate R_{free} labels.

Structure solution and refinement

The Glt$_{Ph}$ structure was phased by molecular replacement in MOLREP (*58*) with 2NWW model (*16*). The initial model was iteratively refined using Coot (*59*) and REFMAC5 (*60*). Crystallographic data statistics are shown in table S1.

Statistical analysis

Simulation data were analyzed with a combination of GROMACS tools and in-house python scripts. Unless stated otherwise, data are given as mean values with errors determined as SD from independent experiments or obtained via bootstrap sampling from simulation data with complete monomeric trajectories treated as independent samples. Experimental kinetic data (Figs. 1D and 5C, and fig. S7, D to F) were analyzed using python scripts and fitted with a monoexponential function using a least squares algorithm; reported errors are SDs obtained using bootstrap sampling. No statistical tests were used.

SUPPLEMENTARY MATERIALS

Supplementary material for this article is available at http://advances.sciencemag.org/cgi/content/full/6/47/eaba9854/DC1

View/request a protocol for this paper from *Bio-protocol*.

REFERENCES AND NOTES

1. R. J. Vandenberg, R. M. Ryan, Mechanisms of glutamate transport. *Physiol. Rev.* **93**, 1621–1657 (2013).
2. C. R. Rose, D. Ziemens, V. Untiet, C. Fahlke, Molecular and cellular physiology of sodium-dependent glutamate transporters. *Brain Res. Bull.* **136**, 3–16 (2018).

3. N. Zerangue, M. P. Kavanaugh, Flux coupling in a neuronal glutamate transporter. *Nature* **383**, 634–637 (1996).

4. M. Groeneveld, D.-J. Slotboom, Na$^+$:Aspartate coupling stoichiometry in the glutamate transporter homologue Glt$_{Ph}$. *Biochemistry* **49**, 3511–3513 (2010).

5. L. M. Levy, O. Warr, D. Attwell, Stoichiometry of the glial glutamate transporter GLT-1 expressed inducibly in a Chinese hamster ovary cell line selected for low endogenous Na$^+$-dependent glutamate uptake. *J. Neurosci.* **18**, 9620–9628 (1998).

6. L. J. DeFelice, T. Goswami, Transporters as Channels. *Annu. Rev. Physiol.* **69**, 87–112 (2007).

7. J.-P. Machtens, D. Kortzak, C. Lansche, A. Leinenweber, P. Kilian, B. Begemann, U. Zachariae, D. Ewers, B. L. de Groot, R. Briones, C. Fahlke, Mechanisms of anion conduction by coupled glutamate transporters. *Cell* **160**, 542–553 (2015).

8. J. C. Jen, J. Wan, T. P. Palos, B. D. Howard, R. W. Baloh, Mutation in the glutamate transporter EAAT1 causes episodic ataxia, hemiplegia, and seizures. *Neurology* **65**, 529–534 (2005).

9. N. Winter, P. Kovermann, C. Fahlke, A point mutation associated with episodic ataxia 6 increases glutamate transporter anion currents. *Brain* **135** (Pt 11), 3416–3425 (2012).

10. P. Kovermann, V. Untiet, Y. Kolobkova, M. Engels, S. Baader, K. Schilling, C. Fahlke, Increased glutamate transporter-associated anion currents cause glial apoptosis in episodic ataxia 6. *Brain Commun.* **2**, fcaa022 (2020).

11. N. Reyes, C. Ginter, O. Boudker, Transport mechanism of a bacterial homologue of glutamate transporters. *Nature* **462**, 880–885 (2009).

12. T. J. Crisman, S. Qu, B. I. Kanner, L. R. Forrest, Inward-facing conformation of glutamate transporters as revealed by their inverted-topology structural repeats. *Proc. Natl. Acad. Sci. U.S.A.* **106**, 20752–20757 (2009).

13. A. A. Garaeva, A. Guskov, D. J. Slotboom, C. Paulino, A one-gate elevator mechanism for the human neutral amino acid transporter ASCT2. *Nat. Commun.* **10**, 3427 (2019).

14. V. Arkhipova, A. Guskov, D. J. Slotboom, Structural ensemble of a glutamate transporter homologue in lipid nanodisc environment. *Nat. Commun.* **11**, 998 (2020).

15. E. Zomot, I. Bahar, Intracellular gating in an inward-facing state of aspartate transporter Glt$_{Ph}$ is regulated by the movements of the helical hairpin HP2. *J. Biol. Chem.* **288**, 8231–8237 (2013).

16. O. Boudker, R. M. Ryan, D. Yernool, K. Shimamoto, E. Gouaux, Coupling substrate and ion binding to extracellular gate of a sodium-dependent aspartate transporter. *Nature* **445**, 387–393 (2007).

17. G. Verdon, S. Oh, R. N. Serio, O. Boudker, Coupled ion binding and structural transitions along the transport cycle of glutamate transporters. *eLife* **3**, e02283 (2014).

18. P. J. Focke, P. Moenne-Loccoz, H. P. Larsson, Opposite movement of the external gate of a glutamate transporter homolog upon binding cotransported sodium compared with substrate. *J. Neurosci.* **31**, 6255–6262 (2011).

19. D. Kortzak, C. Alleva, I. Weyand, D. Ewers, M. I. Zimmermann, A. Franzen, J.-P. Machtens, C. Fahlke, Allosteric gate modulation confers K$^+$ coupling in glutamate transporters. *EMBO J* **38**, e101468 (2019).

20. D. Ewers, T. Becher, J.-P. Machtens, I. Weyand, C. Fahlke, Induced fit substrate binding to an archeal glutamate transporter homologue. *Proc. Natl. Acad. Sci. U.S.A.* **110**, 12486–12491 (2013).

21. I. Hänelt, S. Jensen, D. Wunnicke, D. J. Slotboom, Low affinity and slow Na$^+$ binding precedes high affinity aspartate binding in the secondary-active transporter Glt$_{Ph}$. *J. Biol. Chem.* **290**, 15962–15972 (2015).

22. S. Jensen, A. Guskov, S. Rempel, I. Hänelt, D. J. Slotboom, Crystal structure of a substrate-free aspartate transporter. *Nat. Struct. Mol. Biol.* **20**, 1224–1226 (2013).

23. A. Guskov, S. Jensen, I. Faustino, S. J. Marrink, D. J. Slotboom, Coupled binding mechanism of three sodium ions and aspartate in the glutamate transporter homologue Glt$_{Tk}$. *Nat. Commun.* **7**, 13420 (2016).

24. J. C. Canul-Tec, R. Assal, E. Cirri, P. Legrand, S. Brier, J. Chamot-Rooke, N. Reyes, Structure and allosteric inhibition of excitatory amino acid transporter 1. *Nature* **544**, 446–451 (2017).

25. D. Drew, O. Boudker, Shared molecular mechanisms of membrane transporters. *Annu. Rev. Biochem.* **85**, 543–572 (2016).

26. M. V. LeVine, M. A. Cuendet, G. Khelashvili, H. Weinstein, Allosteric mechanisms of molecular machines at the membrane: Transport by sodium-coupled symporters. *Chem. Rev.* **116**, 6552–6587 (2016).

27. N. Akyuz, R. B. Altman, S. C. Blanchard, O. Boudker, Transport dynamics in a glutamate transporter homologue. *Nature* **502**, 114–118 (2013).

28. H. P. Larsson, X. Wang, B. Lev, I. Baconguis, D. A. Caplan, N. P. Vyleta, H. P. Koch, A. Diez-Sampedro, S. Y. Noskov, Evidence for a third sodium-binding site in glutamate transporters suggests an ion/substrate coupling model. *Proc. Natl. Acad. Sci. U.S.A.* **107**, 13912–13917 (2010).

29. Z. Huang, E. Tajkhorshid, Identification of the third Na$^+$ site and the sequence of extracellular binding events in the glutamate transporter. *Biophys. J* **99**, 1416–1425 (2010).

30. T. Bastug, G. Heinzelmann, S. Kuyucak, M. Salim, R. J. Vandenberg, R. M. Ryan, Position of the third Na$^+$ site in the aspartate transporter Glt$_{Ph}$ and the human glutamate transporter, EAAT1. *PLOS ONE* **7**, e33058 (2012).

31. D. C. Holley, M. P. Kavanaugh, Interactions of alkali cations with glutamate transporters. *Philos. Trans. R. Soc. Lond. B Biol. Sci.* **364**, 155–161 (2009).

32. Z. Tao, N. Rosental, B. I. Kanner, A. Gameiro, J. Mwaura, C. Grewer, Mechanism of cation binding to the glutamate transporter EAAC1 probed with mutation of the conserved amino acid residue Thr^{101}. *J. Biol. Chem.* **285**, 17725–17733 (2010).

33. J. T. Vivian, P. R. Callis, Mechanisms of tryptophan fluorescence shifts in proteins. *Biophys. J.* **80**, 2093–2109 (2001).

34. P. Chakraborty, E. Di Cera, Induced fit is a special case of conformational selection. *Biochemistry* **56**, 2853–2859 (2017).

35. V. I. Gordeliy, R. Schlesinger, R. Efremov, G. Büldt, J. Heberle, Crystallization in lipidic cubic phases: a case study with bacteriorhodopsin. *Methods Mol. Biol.* **228**, 305–316 (2003).

36. N. Reyes, S. Oh, O. Boudker, Binding thermodynamics of a glutamate transporter homolog. *Nat. Struct. Mol. Biol.* **20**, 634–640 (2013).

37. J. Setiadi, S. Kuyucak, Free-energy simulations resolve the low-affinity Na$^+$-high-affinity asp binding paradox in Glt$_{Ph}$. *Biophys. J.* **117**, 780–789 (2019).

38. N. Rosental, B. I. Kanner, A conserved methionine residue controls the substrate selectivity of a neuronal glutamate transporter. *J. Biol. Chem.* **285**, 21241–21248 (2010).

39. N. Silverstein, D. Ewers, L. R. Forrest, C. Fahlke, B. I. Kanner, Molecular Determinants of Substrate Specificity in Sodium-coupled Glutamate Transporters. *J. Biol. Chem.* **290**, 28988–28996 (2015).

40. P. J. Focke, A. W. Annen, F. I. Valiyaveetil, Engineering the glutamate transporter homologue Glt$_{Ph}$ using protein semisynthesis. *Biochemistry* **54**, 1694–1702 (2015).

41. S. Oh, O. Boudker, Kinetic mechanism of coupled binding in sodium-aspartate symporter Glt$_{Ph}$. *eLife* **7**, e37291 (2018).

42. A. Bendahan, A. Armon, N. Madani, M. P. Kavanaugh, B. I. Kanner, Arginine 447 plays a pivotal role in substrate interactions in a neuronal glutamate transporter. *J. Biol. Chem.* **275**, 37436–37442 (2000).

43. E. A. Riederer, F. I. Valiyaveetil, Investigation of the allosteric coupling mechanism in a glutamate transporter homolog via unnatural amino acid mutagenesis. *Proc. Natl. Acad. Sci. U.S.A.* **116**, 15939–15946 (2019).

44. D. E. Bergles, A. V. Tzingounis, C. E. Jahr, Comparison of coupled and uncoupled currents during glutamate uptake by GLT-1 transporters. *J. Neurosci.* **22**, 10153–10162 (2002).

45. H. P. Larsson, A. V. Tzingounis, H. P. Koch, M. P. Kavanaugh, Fluorometric measurements of conformational changes in glutamate transporters. *Proc. Natl. Acad. Sci. U.S.A.* **101**, 3951–3956 (2004).

46. N. Akyuz, E. R. Georgieva, Z. Zhou, S. Stolzenberg, M. A. Cuendet, G. Khelashvili, R. B. Altman, D. S. Terry, J. H. Freed, H. Weinstein, O. Boudker, S. C. Blanchard, Transport domain unlocking sets the uptake rate of an aspartate transporter. *Nature* **518**, 68–73 (2015).

47. M. J. Abraham, T. Murtola, R. Schulz, S. Páll, J. C. Smith, B. Hess, E. Lindahl, GROMACS: High performance molecular simulations through multi-level parallelism from laptops to supercomputers. *SoftwareX* **1-2**, 19–25 (2015).

48. S. Kashefolgheta, A. Vila Verde, Developing force fields when experimental data is sparse: AMBER/GAFF-compatible parameters for inorganic and alkyl oxoanions. *Phys. Chem. Chem. Phys.* **19**, 20593–20607 (2017).

49. M. G. Wolf, M. Hoefling, C. Aponte-Santamaria, H. Grubmüller, G. Groenhof, g_membed: Efficient insertion of a membrane protein into an equilibrated lipid bilayer with minimal perturbation. *J. Comput. Chem.* **31**, 2169–2174 (2010).

50. A. Amadei, A. B. M. Linssen, B. L. de Groot, D. M. F. van Aalten, H. J. C. Berendsen, An efficient method for sampling the essential subspace of proteins. *J. Biomol. Struct. Dyn.* **13**, 615–625 (1996).

51. J. S. Hub, B. L. de Groot, D. van der Spoel, g_wham—A free weighted histogram analysis implementation including robust error and autocorrelation estimates. *J. Chem. Theory Comput.* **6**, 3713–3720 (2010).

52. T. Paramo, A. East, D. Garzón, M. B. Ulmschneider, P. J. Bond, Efficient characterization of protein cavities within molecular simulation trajectories: trj_cavity. *J. Chem. Theory Comput.* **10**, 2151–2164 (2014).

53. R. Briones, C. Blau, C. Kutzner, B. L. de Groot, C. Aponte-Santamaria, GROmaρs: A GROMACS-based toolset to analyze density maps derived from molecular dynamics simulations. *Biophys. J.* **116**, 4–11 (2019).

54. B. S. Selinsky, *Membrane Protein Protocols* (Humana Press Inc., 2003).

55. V. I. Gordeliy, J. Labahn, R. Moukhametzianov, R. Efremov, J. Granzin, R. Schlesinger, G. Büldt, T. Savopol, A. J. Scheidig, J. P. Klare, M. Engelhard, Molecular basis of transmembrane signalling by sensory rhodopsin II-transducer complex. *Nature* **419**, 484–487 (2002).

56. W. Kabsch, XDS. *Acta Crystallogr. D Biol. Crystallogr.* **66**, 125–132 (2010).

57. M. D. Winn, C. C. Ballard, K. D. Cowtan, E. J. Dodson, P. Emsley, P. R. Evans, R. M. Keegan, E. B. Krissinel, A. G. W. Leslie, A. McCoy, S. J. McNicholas, G. N. Murshudov, N. S. Pannu, E. A. Potterton, H. R. Powell, R. J. Read, A. Vagin, K. S. Wilson, Overview of the CCP4 suite and current developments. *Acta Crystallogr. D Biol. Crystallogr.* **67** (Pt 4), 235–242 (2011).

58. A. Vagin, A. Teplyakov, Molecular replacement with *MOLREP. Acta Crystallogr. D Biol. Crystallogr.* **66** (Pt 1), 22–25 (2010).

59. P. Emsley, K. Cowtan, *Coot*: Model-building tools for molecular graphics. *Acta Crystallogr. D Biol. Crystallogr.* **60** (Pt 12 Pt 1), 2126–2132 (2004).

60. G. N. Murshudov, P. Skubák, A. A. Lebedev, N. S. Pannu, R. A. Steiner, R. A. Nicholls, M. D. Winn, F. Long, A. A. Vagin, *REFMAC5* for the refinement of macromolecular crystal structures. *Acta Crystallogr. D Biol. Crystallogr.* **67** (Pt 4), 355–367 (2011).

Citation: C. Alleva, K. Kovalev, R. Astashkin, M. I. Berndt, C. Baeken, T. Balandin, V. Gordeliy, C. Fahlke, J.-P. Machtens, Na$^+$-dependent gate dynamics and electrostatic attraction ensure substrate coupling in glutamate transporters. *Sci. Adv.* **6**, eaba9854 (2020).

Science Advances

Na⁺-dependent gate dynamics and electrostatic attraction ensure substrate coupling in glutamate transporters

C. Alleva, K. Kovalev, R. Astashkin, M. I. Berndt, C. Baeken, T. Balandin, V. Gordeliy, Ch. Fahlke and J.-P. Machtens

ARTICLE TOOLS	http://advances.sciencemag.org/content/6/47/eaba9854
SUPPLEMENTARY MATERIALS	http://advances.sciencemag.org/content/suppl/2020/11/16/6.47.eaba9854.DC1
REFERENCES	This article cites 59 articles, 14 of which you can access for free http://advances.sciencemag.org/content/6/47/eaba9854#BIBL
PERMISSIONS	http://www.sciencemag.org/help/reprints-and-permissions

Use of this article is subject to the Terms of Service